

Intercomparison of methods of coupling between convection and large-scale circulation. 2: comparison over non-uniform surface conditions

Article

Accepted Version

Creative Commons: Attribution 3.0 (CC-BY)

Open Access

Daleu, C. L. ORCID: <https://orcid.org/0000-0003-2075-4902>, Plant, R. S. ORCID: <https://orcid.org/0000-0001-8808-0022>, Woolnough, S. J. ORCID: <https://orcid.org/0000-0003-0500-8514>, Sessions, S., Herman, M. J., Sobel, A., Wang, S., Kim, D., Cheng, A., Bellon, G., Peyrille, P., Ferry, F., Siebesma, P. and van Ulft, L. (2016) Intercomparison of methods of coupling between convection and large-scale circulation. 2: comparison over non-uniform surface conditions. *Journal of Advances in Modeling Earth Systems*, 8 (1). pp. 387-405. ISSN 1942-2466 doi: <https://doi.org/10.1002/2015MS000570> Available at <https://centaur.reading.ac.uk/59328/>

It is advisable to refer to the publisher's version if you intend to cite from the work. See [Guidance on citing](#).

To link to this article DOI: <http://dx.doi.org/10.1002/2015MS000570>

Publisher: American Geophysical Union

including copyright law. Copyright and IPR is retained by the creators or other copyright holders. Terms and conditions for use of this material are defined in the [End User Agreement](#).

www.reading.ac.uk/centaur

CentAUR

Central Archive at the University of Reading

Reading's research outputs online

1 **Intercomparison of methods of coupling between**
2 **convection and large-scale circulation. 2: Comparison**
3 **over non-uniform surface conditions**

C. L. Daleu¹, R. S. Plant¹, S. J. Woolnough², S. Sessions³, M. J. Herman³,

A. Sobel⁴, S. Wang⁵, D. Kim⁶, A. Cheng⁷, G. Bellon⁸, P. Peyrille⁹, F. Ferry⁹,

P. Siebesma^{10,11}, and L. van Ulft¹⁰

4 **Key points.**

- 5 • Tropical convection
6 • Large-scale parameterized dynamics

Correspondence to: C. L. Daleu, c.daleu@reading.ac.uk

¹Department of Meteorology, University

7 **Abstract.** As part of an international intercomparison project, the weak
8 temperature gradient (WTG) and damped gravity wave (DGW) methods
9 are used to parameterize large-scale dynamics in a set of cloud-resolving mod-
10 els (CRMs) and single column models (SCMs). The WTG or DGW method
11 is implemented using a configuration that couples a model to a reference state
12 defined with profiles obtained from the same model in radiative-convective
13 equilibrium. We investigated the sensitivity of each model to changes in SST,
14 given a fixed reference state. We performed a systematic comparison of the
15 WTG and DGW methods in different models, and a systematic comparison
16 of the behavior of those models using the WTG method and the DGW method.

17 The sensitivity to the SST depends on both the large-scale parameteriza-
18 tion method and the choice of the cloud model. In general, SCMs display a
19 wider range of behaviors than CRMs. All CRMs using either the WTG or
20 DGW method show an increase of precipitation with SST, while SCMs show
21 sensitivities which are not always monotonic. CRMs using either the WTG
22 or DGW method show a similar relationship between mean precipitation rate
23 and column-relative humidity, while SCMs exhibit a much wider range of be-
24 haviors. DGW simulations produce large-scale velocity profiles which are smoother
25 and less top-heavy compared to those produced by the WTG simulations.

26 These large-scale parameterization methods provide a useful tool to iden-
27 tify the impact of parameterization differences on model behavior in the pres-
28 ence of two-way feedback between convection and the large-scale circulation.

of Reading, Reading, UK,

1. Introduction

29 A key issue in understanding the tropical climate and its variability is the understand-
30 ing of the two-way interaction between tropical deep convection and large-scale tropical
31 circulations. Numerical models which simultaneously simulate convection and large-scale
32 circulations are computationally expensive due to the large range of spatial scales between
33 individual convective cells and large-scale tropical circulations. Some examples include
34 large-domain, high-resolution simulations as those conducted in projects such as Cascade
35 [e.g., *Holloway et al.*, 2012] and the global cloud-resolving modeling using Nonhydrostatic
36 ICosahedral Atmosphere Model [e.g., *Miura et al.*, 2005].

37 Many single column model (SCM) and cloud-resolving model (CRM) studies have simu-
38 lated the interactions of tropical deep convection with a prescribed large-scale flow, possi-
39 bly based on idealization or experimental campaign [e.g., *Tompkins*, 2001; *Xu et al.*, 2002;
40 *Derbyshire et al.*, 2004; *Petch et al.*, 2006]. In such studies, the time scale characterizing
41 changes in convection is assumed to be short compared to the time scale characterizing
42 changes in the large-scale flow. Simulations with predefined large-scale flow have provided
43 much useful insight. However, the precipitation rates produced are too much constrained
44 due to the predefined large-scale moisture advection [*Mapes*, 1997; *Sobel and Bretherton*,
45 2000] and thus, such simulations cannot be used to understand the factors that con-
46 trol the occurrence and intensity of tropical deep convection [*Sobel et al.*, 2004]. On the
47 other hand, in non-equilibrium conditions there is a close link between convection and

²National Centre for Atmospheric Science,

48 the large-scale flow such that ignoring the feedback of convection on the large-scale flow
49 is not appropriate [*Mapes, 1997; Holloway and Neelin, 2010; Masunaga, 2012*].

50 The two-way interaction between tropical deep convection and large-scale tropical flow
51 has been studied at a reasonable computational cost in both SCMs and CRMs using
52 various forms of parameterized large-scale dynamics. This study compares two methods
53 of parameterized large-scale dynamics—the weak-temperature gradient (WTG) method
54 and the damped gravity wave (DGW) method—in a set of CRMs and SCMs.

55 The WTG method derives the large-scale vertical velocity from buoyancy anomalies. It
56 has been applied to parameterize large-scale tropical circulations that either consume the
57 simulated heating and accordingly maintain zero horizontal temperature gradient [*Sobel*
58 *and Bretherton, 2000*] or remove the horizontal temperature gradient over a short but
59 nonzero time-scale [e.g., *Raymond and Zeng, 2005; Sessions et al., 2010; Daleu et al.,*
60 *2012; Sessions et al., 2015*]. A recent innovation of the WTG method involves spectral
61 decomposition of heating in the vertical dimension [*Herman and Raymond, 2014*]. The
62 DGW method derives the large-scale vertical velocity directly from the approximated mo-
63 mentum equations. It has been applied to study the two-way coupling between convection
64 and large-scale dynamics, with the latter being simplified to a linear gravity wave of a
65 single horizontal wavenumber [*Kuang, 2008, 2011; Wang et al., 2013; Romps, 2012a, b;*
66 *Edman and Romps, 2015*].

67 In the simulations using the WTG or the DGW method the large-scale forcing diagnosed
68 from the domain-mean temperature anomalies induces a moisture source. Therefore, tra-
69 ditional intercomparisons with prescribed large-scale forcing (e.g., TOGA COARE and

Department of Meteorology, University of

70 DYNAMO) and intercomparisons in which moisture source is a relaxation to a prescribed
71 profile [*Derbyshire et al.*, 2004] are extended here to simulations in which convection within
72 the simulated domain feeds back on the large-scale forcing which in turns drives moisture
73 advection. The implementation of the WTG and DGW methods has always used a con-
74 figuration that couples a simulated column to a reference state [e.g., *Raymond and Zeng*,
75 2005; *Sobel et al.*, 2007; *Sessions et al.*, 2010; *Wang and Sobel*, 2011; *Kuang*, 2008, 2011;
76 *Wang and Sobel*, 2012; *Wang et al.*, 2013; *Romps*, 2012a, b] until recently when *Daleu*
77 *et al.* [2012] developed a new configuration that couples two simulated columns via a
78 WTG-derived large-scale circulation [*Daleu et al.*, 2012, 2014]. Much insight has been
79 learned from these efforts. Unfortunately, many aspects of the large-scale parameteriza-
80 tion methods remain uncertain since results using these two large-scale parameterization
81 methods show both similarities and discrepancies in model behavior.

82 In order to understand the different behaviors of these large-scale parameterization
83 methods, this international intercomparison project—the GASS-WTG project—was devel-
84 oped by the Global Energy and Water Exchanges (GEWEX) Global Atmospheric Systems
85 Modelling Panel (GASS). The goals of this project are to develop community understand-
86 ing of the WTG and DGW methods, to identify differences in behavior of SCMs compared
87 to CRMs to inform parameterization development, and to assess the usefulness of these
88 approaches as tools for parameterization development. In this study, we will evaluate
89 the CRMs and SCMs by comparing the strengths of the diagnosed large-scale forcing
90 and the precipitation rates which result from both the model physics and the parame-
91 terized large-scale dynamical feedback. These two-way feedbacks between convection and

Reading, Reading, UK,

92 the large-scale forcing will help us to identify weaknesses in our SCM parameterization
93 schemes and their likely behaviors in general circulation models. However, such compar-
94 ison will be helpful only if a greater consistency is obtained among CRMs than among
95 SCMs.

96 In Part 1 of this study [*Daleu et al.*, 2015], the aim was to understand what causes
97 discrepancies in model behavior when surface conditions in the simulated column are
98 identical to those of the reference state. We implemented the WTG and DGW methods
99 in a set of CRMs and SCMs. For each model, the reference state was defined from
100 profiles obtained in the radiative-convective equilibrium (RCE) simulation of that model.
101 WTG and DGW simulations were performed with the same SST as in the reference state
102 and were initialized with profiles from the reference state. Some models produced an
103 equilibrium state which was almost identical to the corresponding RCE reference state.
104 In contrast, other models developed a large-scale circulation which resulted in either
105 substantially higher or lower precipitation rates in the simulated column compared to
106 the implied value for the RCE reference column. We also explored the sensitivity of
107 the final equilibrium state to the initial moisture conditions. We found that while some
108 models are not sensitive to the initial moisture conditions (independent of the method
109 used to parameterize the large-scale circulation), other models may support two distinct
110 precipitating equilibrium states using either the DGW or WTG method. We also found
111 that some models using the WTG method (but not using the DGW method) can support

³Department of Physics, New Mexico

112 either an equilibrium state with persistent, precipitating convection or an equilibrium
113 state with zero precipitation.

Tech, Socorro, New Mexico, USA,

⁴Department of Environmental Sciences,
Columbia University, New York, New York,
USA,

⁵Department of Applied Physics and
Applied Mathematics, Columbia University,
New York, New York, USA,

⁶Department of Atmospheric Sciences,
University of Washington, Seattle,
Washington, USA,

⁷Climate Science Branch, NASA Langley
Research Centre, Hampton, Virginia, USA,

⁸The Department of Physics, University
of Auckland, Auckland, New Zealand,

⁹Meteo France, Toulouse, France,

¹⁰Royal Netherlands Meteorological
Institute, De Bilt, Netherlands.

¹¹Delft University of Technology, Delft,
Netherlands

114 *Daleu et al.* [2015] revealed some weaknesses of the WTG method. For instance, over
115 uniform SST, the existence of the nonprecipitating equilibrium state in some models
116 was sensitive to the choice of the parameters used in the WTG calculations (e.g., the
117 nominal boundary layer depth). In addition, DGW simulations over uniform SST and
118 with nearly uniform radiative forcing were more likely to reproduce the RCE reference
119 conditions and produced large-scale pressure velocities which were smoother compared
120 to those produced by the WTG simulations. Aside from the choice of the large-scale
121 parameterization method and the details of its implementation, various other factors in
122 the convective models were important for the evolution of convection and its interactions
123 with parameterized large-scale dynamics. For instance, we found that CRMs using either
124 the WTG or DGW method produced broadly similar results, while SCMs produced a
125 much wider range of behaviors.

126 Whilst *Daleu et al.* [2015] considered the case where the simulated column had the
127 same SST as the RCE reference state, this paper focuses on the sensitivity to the SST
128 in the simulated column, which has been a major focus of previous studies using these
129 approaches [e.g., *Raymond and Zeng, 2005; Sobel et al., 2007; Wang and Sobel, 2011*].
130 *Daleu et al.* [2015] used the term “Uniform SST” to refer to conditions in which the
131 simulated column has the same SST as in the RCE reference state. In the present study,
132 we use the same set of CRMs and SCMs presented in *Daleu et al.* [2015] and we use
133 the term “Non-uniform SST” to refer to conditions in which the simulated column has a
134 value of SST which is different to that of the RCE reference state. For each model, we
135 fix the reference state and perform a series of WTG and DGW simulations with a range
136 of SSTs in the simulated column. We perform a systematic comparison of the WTG and

137 DGW methods with a consistent implementation in the models, and also a systematic
138 comparison of the behavior of the models given the same large-scale parameterization
139 method.

140 This paper is organized as follows. Section 2 briefly describes the models that have
141 contributed to this study. Section 3.1 outlines our implementation of the WTG and DGW
142 methods (full details are available in *Daleu et al.* [2015]), while Section 3.2 describes the
143 configurations of our numerical simulations. Section 4 compares the results of the WTG
144 and DGW simulations over non-uniform SSTs. Finally, the conclusions and implications
145 of our study are discussed in section 5.

2. Description of models

146 Six groups participating in this intercomparison study performed simulations with the
147 same set of CRMs and SCMs presented in *Daleu et al.* [2015]. The models are listed in
148 Tables 1 and 2 for CRMs and SCMs, respectively.

2.1. Cloud Resolving Models

149 There are five CRMs, including two in three-dimensions [3-D] and three in two-
150 dimensions [2-D]. The 3-D CRMs are the Weather Research and Forecast model version
151 3.3 (WRF) [*Skamarock et al.*, 2008] and the mesoscale, nonhydrostatic atmospheric model
152 (MesoNH) [*Lafore et al.*, 1997]. The 2-D CRMs are the Langley Research Center Cloud-
153 Resolving Model (LaRC-CRM) [*Cheng and Xu*, 2006], the New Mexico Tech cloud model
154 version 3 (NMTCMv3) introduced in *Raymond and Zeng* [2005], with modifications and
155 enhancements described in *Herman and Raymond* [2014], and the Met Office Large Eddy

156 Model at version 2.4 (LEMv2.4) [*Shutts and Gray, 1994; Petch and Gray, 2001*]. The
157 reader is referred to *Daleu et al. [2015]* for a more complete description of these CRMs.

2.2. Single-Column Models

158 Two pairs of the SCMs come from different versions of the same model. One of the pairs,
159 LMDzA and LMDzB, are the SCM versions of the atmospheric components of IPSL-CM5A
160 and IPSL-CM5B [*Dufresne et al., 2013*]. The other pair, EC-Earthv1 and EC-Earthv3,
161 are SCMs based on the atmospheric general circulation model IFS, cycles 31r1 and 36r4
162 respectively of the European Centre for Medium-Range Weather Forecasts (ECMWF)
163 [*Hazeleger et al., 2010*]. ARPV6 is the SCM version of the atmospheric component of the
164 CNRM-CM, an updated version from that used in CMIP5 [*Voldoire et al., 2013*], GISS-
165 SCM is the SCM version of the National Aeronautics and Space Administration Goddard
166 Institute for Space Studies, an updated version from that used in CMIP5 [*Schmidt et al.,*
167 2014], and UMv7.8 is the SCM version of the UK Met Office Unified Model [*Davies et al.,*
168 2005]. The reader is referred to *Daleu et al. [2015]* for a more complete description of
169 these SCMs.

2.3. Overall approach

170 The CRMs have horizontal domain sizes ranging between 128 and 256 km and hori-
171 zontal resolution ranging between 0.5 and 4 km. The lateral boundary conditions are
172 periodic for all prognostic variables in all CRMs. For CRMs in 2-D, the domain-mean
173 wind speeds in the along-domain direction and in the across-domain direction are relaxed
174 toward vertically uniform values of 0 and 5 m s⁻¹, respectively, both with a relaxation
175 time-scale of 6 h. For fair comparison of 2-D CRM simulations with 3-D CRM simulations

and with SCM simulations, the horizontal domain-mean wind speed components in the 3-D CRMs and SCMs are also relaxed toward vertically uniform values of 0 and 5 m s⁻¹.

For all of these models, the lower boundary condition is a spatially uniform and time-independent SST, and the Coriolis force is zero. We force each model with the idealized cooling profile defined in *Daleu et al.* [2015]. The tendency of temperature due to radiative cooling, $(\partial T/\partial t)_{RC}$, is homogeneous and non-interactive throughout most of the troposphere, and it acts to maintain the temperature toward a fixed value of 200 K at levels with $\bar{p} < 100$ hPa, with a relaxation time scale $\alpha_T^{-1} = 1$ day. That is,

$$\left(\frac{\partial T}{\partial t}\right)_{RC} = \begin{cases} -1.5 & \text{if } \bar{p} \geq 200 \\ -1.5 \left(\frac{\bar{p}-100}{100}\right) - \alpha_T \left(\frac{200-\bar{p}}{100}\right) (\bar{T} - 200) & \text{if } 100 < \bar{p} < 200. \\ -\alpha_T (\bar{T} - 200) & \text{if } \bar{p} \leq 100 \end{cases} \quad (1)$$

3. Parameterization of the large-scale dynamics and experiment setup

3.1. Parameterization of the large-scale dynamics

In the present study, the large-scale circulation is parameterized using two methods: the WTG and DGW methods. As in *Daleu et al.* [2015], the implementation of the WTG or DGW method involves an interactive column that is coupled to a reference state.

A full description of the implementation of the WTG method is given in *Daleu et al.* [2015]. The large-scale pressure velocity, $\bar{\omega}$ between 850 and 100 hPa acts to reduce the difference in the domain-mean virtual potential temperature between the simulated column and the reference state, $\bar{\theta}_v - \bar{\theta}_v^{Ref}$, over a specified time-scale, τ . That is,

$$\bar{\omega} \frac{\partial \bar{\theta}_v^{Ref}}{\partial p} = \frac{\bar{\theta}_v - \bar{\theta}_v^{Ref}}{\tau}. \quad (2)$$

Above 100 hPa $\bar{\omega}$ is set to zero. Below the nominal boundary layer top, 850 hPa, we calculate the values of $\bar{\omega}$ by linear interpolation in pressure from the value diagnosed at the

195 first model level above 850 hPa to zero at the surface. Experiments to assess sensitivities
 196 of the final equilibrium state to the depth of the boundary layer are presented in *Daleu*
 197 *et al.* [2015].

198 A full description of the implementation of the DGW method is given in *Daleu et al.*
 199 [2015]. The second-order derivative of $\bar{\omega}$ is related to the difference in the domain-mean
 200 virtual temperature between the simulated column and the reference state, $\bar{T}_v - \bar{T}_v^{Ref}$, as

$$201 \quad \frac{\partial}{\partial p} \left(\epsilon \frac{\partial \bar{\omega}}{\partial p} \right) = \frac{k^2 R_d}{\bar{p}^{Ref}} (\bar{T}_v - \bar{T}_v^{Ref}), \quad (3)$$

202 where R_d is the gas constant of dry air. ϵ and k are the mechanical damping coefficient
 203 and the horizontal wavenumber, respectively.

204 As in *Daleu et al.* [2015], the large-scale circulation parameterized using either equation 2
 205 or 3 introduces additional source and sink terms to the potential temperature and water
 206 vapor equations only. The prognostic equation for potential temperature includes the
 207 tendency due to vertical advection by the parameterized large-scale circulation. That is,

$$208 \quad \left(\frac{\partial \theta}{\partial t} \right)_{LS} = -\bar{\omega} \frac{\partial \bar{\theta}}{\partial p}. \quad (4)$$

209 The prognostic equation for specific humidity of water vapor (q_v) also includes the large-
 210 scale tendency due to vertical advection, as well as an additional contribution representing
 211 the horizontal advection of the reference state air into the simulated domain by the pa-
 212 rameterized large-scale circulation. That is,

$$213 \quad \left(\frac{\partial q_v}{\partial t} \right)_{LS} = -\bar{\omega} \frac{\partial \bar{q}_v}{\partial p} + \max \left(\frac{\partial \bar{\omega}}{\partial p}, 0 \right) (\bar{q}_v^{Ref} - \bar{q}_v). \quad (5)$$

3.2. Experiment Setup

214 For each model, a radiative-convective equilibrium (RCE) simulation (no large-scale
 215 parameterized dynamics) is first performed over an SST of 300 K. The mean thermody-

216 namic profiles at equilibrium in that simulation are used to define the reference state of
217 that model. We keep the reference state fixed and investigate the sensitivity of the final
218 equilibrium state to the SST in the simulated column as in *Wang and Sobel* [2011].

219 For each of the models listed in Tables 1 and 2, we performed the WTG and DGW
220 simulations of a colder column (using SSTs of 298 and 299.5 K), a warmer column (using
221 SSTs of 300.5, 301, 301.5 and 302 K), and over a uniform SST (using an SST of 300 K;
222 results presented in *Daleu et al.* [2015]). The adjustment time-scale used in the WTG
223 calculations is $\tau = 3$ h. In the DGW calculations, we fix the value of ϵ to 1 day^{-1} and
224 solve equation 3 with a single horizontal wavenumber $k = 10^{-6} \text{ m}^{-1}$. These are typical
225 values used in previous WTG and DGW studies [e.g., *Herman and Raymond*, 2014; *Daleu*
226 *et al.*, 2012; *Wang and Sobel*, 2011; *Wang et al.*, 2013], including *Daleu et al.* [2015]. They
227 have been chosen such that the WTG simulation and the corresponding DGW simulation
228 produce large-scale circulations that are comparable in strength for similar temperature
229 anomalies. The calculations of \bar{w} given by equations 2 and 3 are performed either every
230 10 min (for models with integration time steps smaller or equal to 10 min) or at every
231 model time step (for models with integration time steps greater than 10 min).

232 The results presented in *Daleu et al.* [2015], and in other previous studies [e.g., *Sobel*
233 *et al.*, 2007; *Sessions et al.*, 2010] show that some SCMs and CRMs using the WTG method
234 can sustain either a dry equilibrium state or a precipitating equilibrium state, given suffi-
235 ciently different initial moisture conditions (known as multiple equilibria). Therefore, it is
236 possible that some of our WTG simulations that exhibit precipitating equilibrium states
237 would instead result in dry equilibrium states if initialized with very dry moisture condi-
238 tions. Multiple equilibria and their dependence on parameters in the WTG calculations

239 have already been investigated in *Daleu et al.* [2015], and they are outside the scope of
240 the present paper.

241 The WTG and DGW calculations are initialized with profiles from the models' RCE
242 reference state at 300 K and are allowed to evolve until a new quasi-equilibrium state with
243 parameterized large-scale circulation is reached. The RCE reference profiles differ from
244 model to model, with large differences obtained among SCMs (see Figure 3 in *Daleu et al.*
245 [2015]). The value of surface sensible heat flux also differs between models (not shown)
246 but is much smaller than surface latent heat flux, such that the main balance in the RCE
247 state is between the precipitation rate and the column-integrated radiative cooling rate.
248 Due to the dependence of radiative cooling profile on temperature above 200 hPa (see
249 equation 1), the value of column-integrated radiative cooling rate differs from model to
250 model. The values of mean precipitation rate obtained in the RCE simulations with an
251 SST of 300 K are summarized in the last rows of Tables 1 and 2 for CRMs and SCMs,
252 respectively.

253 We conducted a set of WTG and DGW simulations over non-uniform SSTs using each
254 of the models listed in Tables 1 and 2. The simulations are integrated over different
255 periods of time ranging between 50 and 250 days, as the time-scale of adjustment to a
256 quasi-equilibrium state with the parameterized large-scale circulation differs from model to
257 model and also depends on which large-scale parameterization method is used. The quasi-
258 equilibrium state is reached when a statistically steady state temperature and humidity
259 profiles are achieved when averaged over a long period of time. The mean states and
260 statistics at equilibrium of the simulations to be discussed have been obtained by averaging

261 over the last 20 days in 50-day simulations, 30 days in 100-day simulations, and 100 days
 262 in 250-day simulations.

4. Results

263 In this section, we present the profiles of large-scale pressure velocity and the mean
 264 precipitation rates at equilibrium for different values of SST in the simulated column.
 265 We also present the mean precipitation rates, circulation strength, and column-relative
 266 humidity in a set of scatter plots.

4.1. Parameterized large-scale circulation and mean precipitation rates

267 Figures 1 and 2 show the profiles of \bar{w} obtained at equilibrium in the WTG and DGW
 268 simulations, respectively. Results are shown for all models listed in Tables 1 and 2 and
 269 for SSTs of 298, 299.5, 300 K (uniform SST; results presented in *Daleu et al.* [2015]),
 270 300.5, 301, 301.5 and 302 K. For models in height coordinates, we expressed the large-
 271 scale vertical velocities in Pa s^{-1} by applying the factor “ $-\rho g$,” where ρ is density and g
 272 is the gravitational acceleration.

273 To provide a more quantitative evaluation of the WTG and DGW simulations, we
 274 calculated the ratio of mean precipitation rate in the simulated column, P , to the value
 275 of the corresponding RCE reference state, P_{Ref} . We also calculated the mass-weighted
 276 vertical integral of the large-scale pressure velocities presented in Figures 1 and 2; $\Omega =$
 277 $\int \bar{w} dp / \Delta p$, where Δp is the depth of the troposphere. The numerical values of Ω and
 278 P/P_{Ref} are listed in Tables 3 and 4 for CRMs and SCMs, respectively. Figure 3 shows
 279 P/P_{Ref} as a function of the SST in the simulated column, and Figure 4 shows scatter
 280 plots of Ω versus P/P_{Ref} for all SSTs.

281 4.1.1. Variations between models

282 For a given SST in the simulated column, the characteristic vertical structure of the
283 large-scale circulation at equilibrium differs from model to model, and it also depends
284 on the large-scale parameterization method used. Over an SST of 302 K (red curves in
285 Figures 1 and 2), for example, models using the WTG method exhibit a range of large-
286 scale pressure velocity profiles which vary from unimodal ascent through the column with
287 very top-heavy profiles (e.g., WRF; Figure 1a), to more uniform unimodal profiles (e.g.,
288 LaRC-CRM; Figure 1c), to bi-modal profiles (e.g., EC-Earthv1; Figure 1k), to profiles
289 with distinct minima near the freezing level (e.g., UMv7.8; Figure 1j), including some
290 with weak descent near the freezing level (e.g., GISS-SCM; Figure 1h). As seen in *Daleu*
291 *et al.* [2015], the DGW method produces large-scale pressure velocity profiles which are
292 smoother than those produced using the WTG method (compare Figures 1 and 2).

293 Over cold SSTs (298 and 299.5 K), some models produce large-scale pressure velocity
294 profiles which are insensitive to the SST. In such simulations, convection is inhibited com-
295 pletely and the heating due to the diagnosed large-scale circulation balances the prescribed
296 radiative cooling. Some examples are the WTG simulations of LEMv2.4 with SSTs of 298
297 and 299.5 K which produce zero precipitation rates (see Table 3) and indistinguishable
298 large-scale pressure velocity profiles (see dark blue and light blue curves in Figure 1e).

299 Over warm SSTs, the large-scale pressure velocity profiles and precipitation rates are
300 sensitive to the SST in all the models using either the WTG or DGW method. The
301 sensitivity differs from model to model, and there is much diversity even among CRMs.
302 Using the DGW method, for example, the two 3D CRMs (WRF and MesoNH) with an
303 SST of 302 K produced large-scale pressure velocities and precipitation rates which differ

304 by more than a factor of two (compare the red curves in Figures 2(a) and 2(b), and the
 305 values of P/P_{Ref} in Table 3). However, all CRMs with an SST ≥ 301 K have large-scale
 306 pressure velocities increasing upward to around 400 hPa using the DGW method and to
 307 around 250 hPa using the WTG method.

308 The large-scale pressure velocity profiles produced in most SCM simulations vary con-
 309 siderably from the very top-heavy profiles (e.g., GISS-SCM using the DGW method, see
 310 Figure 2h) through weakly top-heavy profiles (e.g., LMDzB using the WTG method, see
 311 Figure 1g) to the bottom-heavy profiles (e.g., EC-Earthv1 using the WTG method; see
 312 Figure 1k), and some of the pressure velocity profiles show very detailed structures in the
 313 vertical (e.g., UMv7.8 using the WTG method; see Figure 1j). Similar to the results of
 314 *Wang et al.* [2013], the pressure velocity profiles produced using the DGW method are
 315 much smoother and tend to be slightly less top-heavy compared to those produced using
 316 the WTG method (compare Figures 1 and 2).

317 4.1.2. Variations with SST

318 The impact of the SST is readily seen. At SST= 298 K, all the models using either the
 319 WTG or DGW method produce uniform large-scale descent (see the dark blue curves in
 320 Figures 1 and 2). In some of these simulations, the large-scale circulation inhibits pre-
 321 cipitating convection completely (e.g., NMTCMv3 using the DGW method; see Table 3),
 322 while in others an equilibrium state with light precipitation can be achieved (e.g., LMDzB
 323 using the WTG method; see Table 4).

324 At SST= 299.5 K, all CRMs using either the WTG or DGW method produced uniform
 325 large-scale descent. With the exception of GISS-SCM using the WTG method, which
 326 produces large-scale ascent in the upper troposphere (light blue curve in Figure 1h), the

327 SCMs produce either a uniform large-scale descent throughout the column (e.g., ARPV6
328 using the WTG method; light blue curve in Figure 1i) or large-scale descent in the upper
329 troposphere and a very weak circulation in the lower troposphere (e.g., EC-Earthv3 using
330 the WTG method; light blue curve in Figure 1l). The WTG and DGW simulations which
331 produce uniform large-scale descent result in very low precipitation compared to the value
332 of the RCE reference state, consistent with the negative moisture transport implied by
333 the resulting large-scale circulation (e.g., MesoNH using the WTG method; see Table 3),
334 with some simulations producing zero precipitation at equilibrium (e.g., WRF using the
335 WTG method; see Table 3). The WTG and DGW simulations which produce large-scale
336 descent in the upper troposphere and a very weak circulation in the lower troposphere are
337 dominated by shallow convection and thus, result in smaller reductions in precipitation
338 compared to the value of the RCE reference state (e.g., EC-Earthv3 using the WTG
339 method; see Table 4). However, in the WTG simulation of GISS-SCM with an SST of
340 299.5 K the mean precipitation rate at equilibrium is slightly increased (with respect to
341 the value of the RCE reference state) to balance the net small cooling produced by the
342 large-scale ascent in the upper troposphere. In contrast, the DGW simulation of GISS-
343 SCM with an SST of 299.5 K produces a different sign of the circulation with a reduction
344 of precipitation (see Table 4).

345 The results of the WTG and DGW simulations over uniform SST are presented in
346 *Daleu et al.* [2015]. There, we considered that a WTG or DGW simulation over a uniform
347 SST replicated the corresponding RCE reference state to a good approximation if $0.9 <$
348 $P/P_{Ref} < 1.1$ and $-0.4 \times 10^{-2} < \Omega < 0.4 \times 10^{-2} \text{ Pa s}^{-1}$. The values of Ω and P/P_{Ref}
349 for such simulations are both bold-faced in Tables 3 and 4. Some models replicate the

350 corresponding RCE reference state to a good approximation. In contrast, other models
351 sustain a large-scale ascent (or descent) which results in substantially higher (or lower)
352 precipitation rate in the simulated column compared to the value of the corresponding
353 RCE reference state.

354 Those models which produce a lower precipitation rate over a uniform SST of 300 will
355 not produce a mean precipitation rate which is equivalent to the value of the RCE reference
356 state unless the SST in the simulated column is increased, consistent with the results of
357 *Raymond and Zeng* [2005]. An example is UMv7.8 using the WTG method (see P/P_{Ref}
358 as a function of the SST; green curve in Figure 3b). Similarly, models which produce a
359 higher precipitation rate will not produce a mean precipitation rate which is equivalent to
360 the value of the RCE reference state unless the SST in the simulated column is decreased
361 (e.g., AR Pv6 using the WTG method; solid black curve in Figure 3b).

362 An SST of 300.5 K results in substantially higher precipitation rate ($P/P_{Ref} > 1.1$)
363 in all the WTG and DGW simulations, except EC-Earthv1. A large proportion of these
364 simulations produce uniform large-scale ascent (e.g., GISS-SCM using the DGW method,
365 dark green curve in Figure 2h). Other simulations produce large-scale circulations with
366 a layer of descent near the freezing layer, but which nonetheless result in net column-
367 integrated cooling and moistening of the simulated column (e.g., AR Pv6 using the WTG
368 method, dark green curve in Figure 1i and $P/P_{Ref} > 1.1$ in Table 4). In contrast, the
369 WTG and DGW simulations of EC-Earthv1 with an SST of 300.5 K produce large-scale
370 circulations with ascent in the upper troposphere and descent in the lower troposphere
371 (dark green curves in Figures 1k and 2k), despite producing ascent in the lower troposphere
372 over a uniform SST of 300 K (black curves in Figures 1k and 2k). In this model using

373 the DGW method, the large-scale circulation cools and moistens the upper troposphere
374 at the same rates as it warms and dries the the lower troposphere. As a result, the
375 column-integrated heating and moistening rates produced by the large-scale circulation
376 are both negligible and thus, the simulated column achieves an equilibrium precipitation
377 rate which is very close to the corresponding RCE reference state (see value of P/P_{Ref}
378 in Table 4). In contrast, using the WTG method the upper tropospheric cooling and
379 moistening do not prevent a reduction in precipitation rate due to the lower tropospheric
380 warming and drying (see Table 4). A similar result is obtained in the WTG simulation
381 of EC-Earthv1 with an SST of 301 K (see the light green curve in Figure 1k and and the
382 value of P/P_{Ref} in Table 4). The WTG and DGW simulations of EC-Earthv1 with an
383 SST of 301 K produce different signs of the integrated circulation.

384 At SSTs > 301 K, the mean precipitation rate is increased compared to the value
385 of the corresponding RCE reference state in all the models using either the WTG or
386 DGW method. These simulations produce uniform large-scale ascent in the simulated
387 column, with the exceptions of the WTG simulations of ARPV6 and GISS-SCM, in which
388 a thin layer of descent between 750 and 650 hPa does not prevent an increase in mean
389 precipitation rate.

390 For all CRMs using either the WTG or the DGW method the simulated column evolves
391 toward a new quasi-equilibrium state with mean precipitation rate increasing non-linearly
392 with SST, consistent with SCM results from *Sobel and Bretherton* [2000], and *Ramsay*
393 *and Sobel* [2011]. In contrast, the SCMs show sensitivities of the mean precipitation rate
394 to the SST which are not always monotonic (e.g., EC-Earthv1 using either the WTG or
395 DGW method; solid red curves in Figures 3b and 3d).

396 Within an individual model, the sensitivity of precipitation rate to the SST depends
 397 on which large-scale parameterization method is used. An example is WRF which shows
 398 a stronger sensitivity under the DGW method than under the WTG method (compared
 399 the dashed curves in Figures 3a and 3c). On the other hand, given one of the large-
 400 scale parameterization methods (either the WTG or DGW method), the sensitivity of
 401 precipitation rate to the SST differs from model to model.

402 An approximately linear relationship between Ω and the mean precipitation rate is
 403 expected, since the mean vertical motion and mean vertical moisture advection are cor-
 404 related. In our study, despite the differences in the pressure velocity profiles, Ω and the
 405 mean precipitation rate show a fairly linear relationship (see Figure 4) and only models
 406 with unusual vertical pressure velocity profiles shows deviations from this linear relation-
 407 ship (e.g., GISS-SCM using the WTG method; see Figure 1h and circles in Figure 4b).
 408 Most of the models meet the expectation that the large-scale circulation and precipitation
 409 rate should increase with SST. Models which show a monotonic increase of precipitation
 410 with SST also show a monotonic increase of precipitation with Ω (WRF using the WTG
 411 method; dashed curve with solid circles in Figure 3a and solid circles in Figure 4a). In con-
 412 trast, models which show a non monotonic increase of precipitation with SST also show a
 413 non monotonic increase of precipitation with Ω (e.g., GISS-SCM using the WTG method
 414 at warm SSTs; dashed black curve with circles in Figure 3b and circles in Figure 4b).

4.2. Precipitation and Column relative humidity

415 In this section, we examine the relationship between precipitation and the column rela-
 416 tive humidity (hereafter CRH) in our WTG and DGW simulations. CRH is calculated as
 417 the ratio of column-integrated water vapor to its saturation value. Figure 5 shows scatter

418 plots of P versus CRH . It also shows the exponential fit for the observed monthly mean
 419 precipitation over the tropical oceans obtained by *Bretherton et al.* [2004](solid curve).

420 That is

$$421 \quad P(\text{mmd}^{-1}) = \exp[11.4(CRH - 0.522)]. \quad (6)$$

422 To account for the variations in CRH of the RCE reference state, we also consider Figure 6,
 423 which shows scatter plots of the ratios P/P_{Ref} versus CRH/CRH_{Ref} , where CRH_{Ref} is
 424 the column-integrated relative humidity of the RCE reference state. The values of P and
 425 CRH are those obtained at equilibrium in the WTG and DGW simulations of each of the
 426 models listed in Tables 1 and 2 with the values of SST ranging between 298 and 302 K.

427 Generally, the mean precipitation rate increases as CRH increases, except in the DGW
 428 simulations of LMDzA with SSTs ≤ 300.5 K in which CRH decreases while precipitation
 429 rate increases (see left facing triangles in Figure 5d). The decrease of CRH with mean
 430 precipitation rate is unusual, but we do not investigate this further in this study.

431 In a large proportion of the models, there is a threshold value of CRH below which
 432 there is virtually no precipitation or strongly reduced precipitation rate (with respect to
 433 the value of the RCE reference state) and above which precipitation rate rapidly increases
 434 with CRH . Below this threshold, the WTG and DGW simulations show changes in
 435 mean precipitation rate that are relatively small for large changes in CRH . Above this
 436 threshold, a significant increase in precipitation rate is obtained, followed by a sharp
 437 pickup of mean precipitation rate as CRH increases further. The value of this threshold
 438 varies from one model to another and it also depends on the large-scale parameterization
 439 method used.

440 These relationships between CRH and mean precipitation rate are qualitatively similar
 441 to that seen in observations over the tropical ocean regions [*Bretherton et al.*, 2004] (see
 442 solid curves in Figure 5), and in other idealized models [e.g., *Raymond and Zeng*, 2005;
 443 *Wang and Sobel*, 2011], but there are significant quantitative differences. For instance,
 444 CRMs using either the WTG or DGW method produce similar relationship between P
 445 and CRH . However, all CRMs using either the WTG or DGW method have a higher
 446 threshold than observations and their mean precipitation rates rise more abruptly with
 447 CRH than in observations (see Figures 5a and 5c). In contrast, SCMs show a much
 448 larger variety of relationships (see Figures 5b and 5d). Moreover, the transition from
 449 near zero precipitation to rapid increase in precipitation with CRH is sharper in some
 450 models compared to others (e.g., compare P versus CRH in the WTG simulations of
 451 UMv7.8 and LMDzB; stars and right facing triangles in Figure 5b, respectively). When
 452 P and CRH are scaled by their reference values (see Figure 6), the CRMs produce a
 453 relatively tight relationship. The spread among SCMs is also clearly reduced, although
 454 considerable scatter remains. In general, the threshold occurs at around CRH_{Ref} and
 455 beyond that, P increases much more rapidly with CRH in CRMs than in SCMs.

4.3. Budget analysis

456 As in *Daleu et al.* [2015], we analyze the budgets in order to clarify the differences
 457 among RCE, WTG, and DGW simulations. For a simulation with parameterized large-
 458 scale circulation, the heat and moisture budgets are written as

$$459 \quad H + P + R + H_{LS} = 0 \quad \text{and} \quad E - P + M_{LS} = 0, \quad (7)$$

460 respectively. E , H , P and R denote the domain and time-averaged values of surface
 461 evaporation, surface sensible heat flux, precipitation rate and vertically integrated radia-
 462 tive cooling rate respectively. The heating rate and moistening rate due to the diagnosed
 463 large-scale circulation ($H_{LS} = C_p \langle \partial \bar{T} / \partial t \rangle_{LS}$ and $M_{LS} = L_v \langle \partial \bar{q} / \partial t \rangle_{LS}$, respectively) are
 464 zero by definition for the RCE simulations. C_p is the heat capacity at constant pressure
 465 and L_v is the latent heat of vaporization.

466 From the moisture budget equation, the changes in mean precipitation rate with respect
 467 to the value of the RCE reference state, ΔP , must be due to changes in surface evaporation
 468 with respect to the value of the RCE reference state, ΔE , and/or the moistening rate due
 469 to the large-scale circulation M_{LS} . Figures 7 and 8 show scatter plots of ΔP versus M_{LS}
 470 and scatter plots of ΔP versus ΔE , respectively.

471 Both CRMs and SCMs show fairly linear relationships between ΔP and M_{LS} . However,
 472 the slope is not one-to-one (dotted oblique line in Figure 7), which implies changes in
 473 surface evaporation as shown in Figure 8. ΔE increases with ΔP in a large proportion
 474 of the WTG and DGW simulations, and there are only a few simulations which show
 475 an enhancement of convective activity associated with a reduction in surface evaporation
 476 (e.g., WTG simulation of LaRC-CRM an SST of 300.5 K, dark green solid diamond in
 477 Figure 8a) or which show a suppression in convective activity associated with an increase
 478 in surface evaporation (e.g., the WTG simulation of EC-Earthv1 with SST of 300.5 K,
 479 dark green diamond in Figure 8b).

480 The sensitivity of surface fluxes (sum of sensible heat and latent heat fluxes) to changes
 481 in near-surface perturbation winds due to changes in convective activity has been some-
 482 what constrained in this study by imposing a mean horizontal wind speed in the surface

483 flux calculations. As a result, ΔE is generally much smaller than ΔP , such that changes
 484 in precipitation are largely balanced by the large-scale moistening rates. This is readily
 485 seen in Figures 7 and 8. For a large proportion of the simulations, the values of M_{LS} are
 486 about or more than two third the values of ΔP .

487 We now examine the relationship between ΔP and the normalized gross moist stability
 488 (NGMS), Γ . Γ is defined as the dimensionless number which relates the net lateral outflow
 489 of moist static energy from a convective region to a measure of the strength of convection
 490 in that region [Raymond *et al.*, 2009]. That is

$$491 \quad \Gamma = -\langle \bar{\omega} \partial \bar{h} / \partial p \rangle / L_v \langle \bar{\omega} \partial \bar{q}_v / \partial p \rangle, \quad (8)$$

492 where h is the moist static energy. Following Daleu *et al.* [2015],

$$493 \quad \Gamma = -(M_{LS} + H_{LS}) / M_{LS}, \quad (9)$$

494 and a diagnostic equation for ΔP is

$$495 \quad \Delta P = \frac{\Gamma + 1}{\Gamma} \Delta E + \frac{\Delta H + \Delta R}{\Gamma}, \quad (10)$$

496 where ΔH and ΔR are respectively the changes in surface sensible heat flux and column-
 497 integrated radiative cooling rates with respect to the values of the RCE reference state.

498 The reader is referred to Daleu *et al.* [2015] for a derivation of equation 10.

499 As discussed above, ΔH is much smaller than ΔP . ΔR is also much smaller than ΔP as
 500 a result of imposing a fixed radiative cooling profile throughout most of the troposphere.
 501 Also, most of these simulations show that the sum of ΔH and ΔR is much smaller than
 502 ΔE , such that the factor $(\Gamma + 1)/\Gamma$ largely describes the strength of the relationship
 503 between ΔP and ΔE (see equation 10).

504 For the WTG and DGW simulations which reproduce the RCE reference state to a
 505 good approximation, Γ is a poor diagnostic since $M_{LS} + H_{LS}$ and M_{LS} are both close to
 506 zero, consistent with a weak large-scale circulation. Moreover, Γ measures the efficiency
 507 of convection in removing moisture static energy from the column and thus, is not a
 508 particularly useful diagnostic when convection is strongly suppressed. Therefore, the
 509 values of Γ for the WTG and DGW simulations which result in significant large-scale
 510 descent are not relevant, and we consider Figure 9, which shows Γ as a function of SST
 511 for the WTG and DGW simulations which result in significant large-scale ascent only.
 512 These are simulations which produce $P/P_{Ref} > 1.1$ with $\Omega > 0.4 \times 10^{-2} \text{ Pa s}^{-1}$.

513 Most CRM simulations which result in significant large-scale ascent have positive values
 514 of Γ and the WTG and DGW simulations of LaRC-CRM with an SST of 300.5 K are
 515 the only CRM simulations which have negative values of Γ (black diamonds in Figures 9a
 516 and 9c). Among SCMs, simulations with warm SSTs which produce significant large-scale
 517 ascent have positive values of Γ . Negative Γ in some SCMs are obtained in the simulations
 518 which result in either large-scale ascent over a cold SST (e.g., the WTG of GISS-SCM
 519 with an SST of 299.5 K; Table 4 and black circles in Figure 9b) or large-scale ascent
 520 over a uniform SST (e.g., the WTG and DGW simulations of EC-Earthv1 and the DGW
 521 simulation of ARPV6 over a uniform SST of 300 K; Table 4 and red diamonds in Figures 9b
 522 and 9d, and black down facing triangles in Figures 9d). In the simulations which result
 523 in significant large-scale ascent and have negative values of Γ , M_{LS} values are positive.
 524 Therefore, negative values of Γ are the result of a deficit of cooling over moistening rates.
 525 That implies a reduction in evaporation despite an increase in precipitation rate in those
 526 simulations (e.g., dark green diamond in Figures 8a and c). With the exception of the

527 negative values of Γ , Γ generally ranges between 0 and 1, with only few SCM simulations
 528 having $\Gamma > 1$ (e.g., LMDzA using the DGW with an SST of 300.5 K; blue left facing
 529 triangles in Figure 9d).

530 CRMs (except LaRC-CRM) and three SCMs (EC-Earthv3, UMv7.8 and LMDzB) using
 531 either the WTG or DGW method have Γ which is relatively insensitive to the SST. In
 532 those models, ΔE , and hence M_{LS} scale approximately linearly with ΔP . In the other
 533 four SCMs and LaRC-CRM, Γ show large sensitivity including non-monotonic behaviour,
 534 and there are substantial differences in the relationship between Γ and SST depending on
 535 which large-scale parameterization is used (e.g., compare Γ versus SST for the WTG and
 536 DGW simulations of ARpv6; down facing triangles in Figures 9b and 9d).

537 In this study, there is no straightforward relation between Γ and the top-heaviness of
 538 \bar{w} calculated as the mass-weighted vertical integral of the pressure velocity over the layer
 539 at 500 – 100 hPa (see definition in Section 4.1). In addition, Γ does not explain the
 540 difference between different models sensitivity to SST. Despite the fact that studies of
 541 this nature allow convection to interact with the large-scale dynamics, there are many
 542 differences between these feedbacks compared to full General Circulation Models (GCMs)
 543 and the real tropical circulations. For instance, evaporation is not tied to the large-scale
 544 circulation, the moisture convergence is directly tied to the dynamical convergence without
 545 any contribution from the rotational part of the flow, and radiation is non interactive.
 546 Therefore, the NGMS in these studies may have very different characteristics compared
 547 to that of full GCMs and the real tropical circulations.

548 On the other hand, *Wang and Sobel* [2011] idealize horizontal moisture convergence and
 549 radiation in the same way as in our study and found that Γ is a predictor of ΔP in the

precipitating regime. In this study, only two models exhibit positive values of Γ which
 are a monotonically decreasing function of SST or P as in *Wang and Sobel* [2011]. These
 models are WRF and LEMv2.4 using either the WTG or DGW method (circles and down
 facing triangles in Figures 9a and 9c). In contrast to the result of *Wang and Sobel* [2011],
 some models exhibit positive values of Γ which are a monotonically increasing function of
 SST or P (e.g., AR Pv6 using the WTG method with warm SSTs, down facing triangles
 in Figure 9b) while other models exhibit positive or negative values of Γ which are not
 directly related to SST or P (e.g., LaRC-CRM using the DGW method with warm SSTs,
 diamonds in Figure 9c). In the latter case, Γ and ΔE are both important to predict ΔP
 (see equation 10).

5. Conclusions

In this international intercomparison project, we used the WTG and DGW methods to
 study the two-way interaction between convection and large-scale circulations in various
 CRMs and SCMs. Using the WTG method we derived the large-scale circulation that
 reduces the virtual potential temperature anomalies over a given time-scale [*Raymond
 and Zeng, 2005; Sobel et al., 2007; Sessions et al., 2010; Daleu et al., 2012*], and using
 the DGW we simplified the large-scale circulation to a linear gravity wave of a single
 horizontal wave number [*Kuang, 2008, 2011; Romps, 2012a, b*]. In both cases, the derived
 large-scale circulation couples a model to a reference state defined with profiles generated
 from previous RCE simulations of the same model. In *Daleu et al.* [2015], we analysed
 WTG and DGW simulations over a uniform SST. In this paper, we kept the reference
 state fixed and conducted WTG and DGW simulations with different values of SST in
 the simulated column.

572 The WTG and DGW simulations with a cold (or a warm) SST result in lower (or higher)
573 precipitation rates (compared to the value of the RCE reference state) in all CRMs and
574 in a large proportion of the SCMs. In a few SCMs, a WTG simulation over a warm
575 SST and a corresponding DGW simulation produce different signs of the circulation. In
576 those SCMs, different signs of the circulation occur because the WTG simulation produces
577 large-scale ascent over a cold SST or large-scale descent over a warm SST.

578 In general, the behavior across models for a given large-scale parameterization method
579 is different, and the behavior of an individual model also depends on which large-scale
580 parametrization is used. However, DGW simulations do produce large-scale pressure ve-
581 locity profiles which are smoother than those produced by WTG simulations, and consis-
582 tent with the results of *Wang et al.* [2013], DGW simulations generally produce large-scale
583 pressure velocity profiles which are less top-heavy compared to those produced by WTG
584 simulations.

585 All CRMs and five out of the seven SCMs show a monotonic increase of mean precipi-
586 tation rate with SST using either the WTG or DGW method. A similar relationship
587 between precipitation rate and SST was produced in *Sobel and Bretherton* [2000] and
588 *Ramsay and Sobel* [2011]. The other two SCMs show sensitivity of the mean precipitation
589 rate with SST which is not always monotonic. CRMs show a fairly linear relationship
590 between mean precipitation rate and the amplitude of the diagnosed vertically-integrated
591 large-scale circulation, while a few SCMs show deviations from this linear relationship,
592 particularly for simulations with warm SST.

593 Precipitation is an increasing function of the column relative humidity, with the former
594 increasing rapidly as the latter passes a threshold. A similar relationship is found in other

595 numerical modeling studies [*Wang and Sobel, 2011; Raymond and Zeng, 2005*], and is
596 consistent with observations [*Bretherton et al., 2004; Holloway and Neelin, 2009*]. All
597 CRMs using either the WTG or DGW method show a similar relationship between mean
598 precipitation rate and column-relative humidity. They are all moister and the resulting
599 mean precipitation rate increases more abruptly with column relative humidity than in
600 observations. SCMs show a much wider range of relationships between precipitation rate
601 and column-relative humidity, although this spread is reduced when values are normalized
602 by their RCE values.

603 In our WTG and DGW simulations, the change in precipitation with respect to the
604 value of the RCE reference column is largely balanced by the moistening rate due to the
605 large-scale circulation. We calculated the NGMS for simulations with significant large-
606 scale ascent at equilibrium. A large proportion of those simulations exhibited positive
607 values of NGMS, ranging between 0 and 1, and only a few simulations exhibit negative
608 values of NGMS or values of NGMS that approach 1.5. Those which exhibit negative
609 values of NGMS have a deficit of cooling over moistening rates, which implies a reduction
610 in evaporation despite an increase in precipitation rate. Most CRMs and three SCMs
611 using either the WTG or DGW method show small sensitivity of the NGMS with the
612 SST. In the other CRM and the other four SCMs the relationship between NGMS and
613 SST varies considerably and depends on the large-scale parameterization method used.
614 In this study Γ is not related to the shape of the large-scale pressure velocity profile
615 and does not explain the difference between different model's sensitivity to SST. That
616 is, in comparison to real tropical circulations, the NGMS in this configuration may not

617 be a very important diagnostic due to the way in which evaporation, horizontal moisture
618 convergence and radiation are idealized.

619 In this intercomparison project convection feeds back on the large-scale forcing, the
620 moisture source is induced by the derived large-scale motion, and the precipitation rate
621 produced is the result of both the model physics and parameterized large-scale dynamical
622 feedback. Therefore, this study can be viewed as an extension of traditional intercom-
623 parisons with prescribed large-scale forcing (e.g., TOGA COARE and DYNAMO) and
624 intercomparisons in which moisture source is defined as a relaxation to a prescribed pro-
625 file [Derbyshire *et al.*, 2004]. The results from this intercomparison project are important
626 for understanding the two-way interaction between convection and large-scale tropical
627 dynamics and also for interpreting discrepancies between the results reported in the lit-
628 erature. Our results suggested that the discrepancies between the published results can
629 be related to the choice of the large-scale parameterization method. For instance, we
630 found that an individual model can produce different equilibrium states depending on the
631 large-scale parameterization method used.

632 Moreover, we found that even with exactly the same implementation of the WTG
633 or DGW method, different SCM and even CRM models produce different sensitivities
634 of the equilibrium state to SST. CRMs that participated in this study differ in their
635 representation of subgrid scale processes that are important for the evolution of convection
636 and its interaction with large-scale circulation (e.g., cloud microphysics) . The differences
637 in CRMs lead to some diversity of behavior in RCE simulations [Daleu *et al.*, 2015],
638 and the diversity of behavior can be amplified when the physics is allowed to interact
639 with the large-scale dynamics. However, despite the diversity obtained among CRMs, our

640 study demonstrates much larger inter-model variability among SCMs. That is, despite the
641 significant differences in CRMs (e.g., resolution, domain size, microphysics and etc), the
642 behaviour of these simulations using models with explicit convection are more constrained
643 than those with parameterized convection.

644 This study has evaluated CRM and SCM sensitivities to parameterized large-scale
645 dynamical feedback with fixed radiation and a non interactive surface. Further study
646 may compare models and large-scale parameterization methods with interactive radiation
647 and/or an interactive surface. Since our study indicates that there is a greater consistency
648 in the behavior of CRMs under parameterized large-scale circulation while SCMs produce
649 a much larger variation of behaviors, comparison between CRM and SCM behavior under
650 parameterized large-scale circulation may be a useful tool when developing and testing
651 parameterization schemes. Therefore, further analysis may be to assess the impact of
652 changes in parameterization within a particular SCM.

653 **Acknowledgments.** C.L.D., R.S.P., and S.J.W. thank the UK Met Office for the
654 availability of the LEM at version 2.4 and SCM version 7.8 of the UK Met Office Unified
655 Model. C.L.D. was supported by NERC, grant NE/K004034/1. S.J.W. was supported
656 by the NCAS, a NERC collaborative center. The New Mexico Tech group thanks Carlos
657 Lopez Carrillo, Ana Juračić, and Stipo Sentić for model output analysis and for con-
658 tinual discussions on the tropical atmosphere. We also thank Raúl Morales-Juberías for
659 use of the Pelican beowulf cluster. S.L.S. acknowledges support from U.S. National Sci-
660 ence Foundation Grants AGS-1056254 and AGS-1342001, and NM EPSCoR. M.J.H. was
661 supported by U. S. National Science Foundation Grant 1342001. A.H.S .and S.W. were
662 partially supported by NSF grant AGS-1062206. The WRF simulations were carried out

663 on the Yeti Shared HPC Cluster at Columbia University. G.B. thanks Isabelle Beau, An-
664 toinette Alias, David Saint-Martin, Jean-Yves Grandpeix, Marie-Pierre Lefebvre and the
665 CNRS/INSU-LEFE project DEPHY and the European Union FP7 project EMBRACE.
666 D.K. appreciates the NASA/GISS modeling group, especially Maxwell Kelley, Mao-Sung
667 Yao, and Anthony Del Genio, for their invaluable and unlimited supports. D.K. and
668 A.H.S. were supported by the NASA grant NNX13AM18G and the Korea Meteorologi-
669 cal Administration Research and Development Program under Grant CATER 2013-3142.
670 LaRC CRM-IPHOC was partially supported by DOE Atmospheric System Research Pro-
671 gram under Interagency agreements DE-SC0005450 and DE-SC0008779. The computa-
672 tion resources were provided by SSAI Icluster and LaRC Kcluster. P.P., A.P.S. and L.U.
673 were supported by the European Commissions Seventh Framework Programme, under
674 Grant Agreement number 282672, EMBRACE project. Data used for this research are
675 available upon request from the corresponding author; please send requests via email to
676 c.daleu@reading.ac.uk.

References

- 677 Bretherton, C., P. Blossey, and M. Khairoutdinov (2005), An energy-balance analysis of
678 deep convective self-aggregation above uniform SST, *J. Atmos. Sci.*, *62*, 4273–4292.
- 679 Bretherton, C. S., M. E. Peters, and L. E. Back (2004), Relationships between water
680 vapor path and precipitation over the tropical ocean, *J. Clim.*, *17*, 1517–1528.
- 681 Cheng, A., and K.-M. Xu (2006), Simulation of shallow cumuli and their transition to
682 deep convective clouds by cloud-resolving models with different third-order turbulence
683 closures, *Q. J. R. Meteorol. Soc.*, *132*, 359–382.

- 684 Daleu, C., S. Woolnough, and R. Plant (2012), Cloud-resolving model simulations with
685 one and two-way couplings via the weak-temperature gradient approximation, *J. Atmos.*
686 *Sci.*, *69*, 3683–3699.
- 687 Daleu, C., S. Woolnough, and R. Plant (2014), Transition from suppressed to active
688 convection modulated by a weak-temperature gradient derived large-scale circulation,
689 *J. Atmos. Sci.*, *72*, 834–853.
- 690 Daleu, C., et al. (2015), Intercomparison of methods of coupling between convection and
691 large-scale circulation: I. comparison over uniform surface conditions, *J. Adv. Model.*
692 *Earth. Syst.*
- 693 Davies, T., M. Cullen, A. Malcolm, M. Mawson, A. Staniforth, A. White, and N. Wood
694 (2005), A new dynamical core for the Met Office’s global and regional modelling of the
695 atmosphere, *Q. J. R. Meteorol. Soc.*, *131*, 1759–1782.
- 696 Derbyshire, S., I. Beau, P. Bechtold, J. Grandpeix, J. Piriou, J. Redelsperger, and
697 P. Soares (2004), Sensitivity of moist convection to environmental humidity, *Q. J. R.*
698 *Meteorol. Soc.*, *130*, 3055–3079.
- 699 Dufresne, J.-L., et al. (2013), Climate change projections using the IPSL-CM5 earth
700 system model: From CMIP3 to CMIP5, *Clim. Dyn.*, *40*, 2123–2165.
- 701 Edman, J. P., and D. M. Romps (2015), Self-consistency tests of large-scale dynamics
702 parameterizations for single-column modeling, *J. Adv. Model. Earth. Syst.*, *7*, 320–334.
- 703 Hazeleger, W., et al. (2010), EC-Earth: A seamless earth-system prediction approach in
704 action, *Bull. Am. Meteorol. Soc.*, *91*, 1357–1363.
- 705 Herman, M. J., and D. J. Raymond (2014), WTG cloud modeling with spectral decom-
706 position of heating, *J. Adv. Model. Earth. Syst.*, *6*, 1121–1140.

707 Holloway, C., S. Woolnough, and G. Lister (2012), Precipitation distributions for explicit
708 versus parametrized convection in a large-domain high-resolution tropical case study,
709 *Q. J. R. Meteorol. Soc.*, *138*, 1692–1708.

710 Holloway, C. E., and J. D. Neelin (2009), Moisture vertical structure, column water vapor,
711 and tropical deep convection, *J. Atmos. Sci.*, *66*, 1665–1683.

712 Holloway, C. E., and J. D. Neelin (2010), Temporal relations of column water vapor and
713 tropical precipitation, *J. Atmos. Sci.*, *67*, 1091–1105.

714 Kuang, Z. (2008), Modeling the interaction between cumulus convection and linear grav-
715 ity waves using a limited-domain cloud system-resolving model, *J. Atmos. Sci.*, *65*,
716 576–591.

717 Kuang, Z. (2011), The wavelength dependence of the gross moist stability and the scale
718 selection in the instability of column-integrated moist static energy, *J. Atmos. Sci.*, *68*,
719 61–74.

720 Lafore, J. P., et al. (1997), The Meso-NH atmospheric simulation system. Part I: Adi-
721 abatic formulation and control simulations, in *Ann. Geophys*, vol. 16, pp. 90–109,
722 Springer.

723 Mapes, B. (1997), Equilibrium vs. activation control of large-scale variations of tropical
724 deep convection, *The physics and parameterization of moist atmospheric convection*, pp.
725 321–358.

726 Masunaga, H. (2012), A satellite study of the atmospheric forcing and response to moist
727 convection over tropical and subtropical oceans, *J. Atmos. Sci.*, *69*, 150–167.

728 Miura, H., H. Tomita, T. Nasuno, S.-i. Iga, M. Satoh, and T. Matsuno (2005), A climate
729 sensitivity test using a global cloud resolving model under an aqua planet condition,

730 *Geophys. Res. Lett.*, *32*.

731 Pauluis, O., and S. Garner (2006), Sensitivity of radiative-convective equilibrium simu-
732 lations to horizontal resolution, *J. Atmos. Sci.*, *63*, 1910–1923.

733 Petch, J., and M. Gray (2001), Sensitivity studies using a cloud-resolving model simula-
734 tion of the tropical west Pacific, *Q. J. R. Meteorol. Soc.*, *127*, 2287–2306.

735 Petch, J., A. Brown, and M. Gray (2006), The impact of horizontal resolution on the
736 simulations of convective development over land, *Q. J. R. Meteorol. Soc.*, *132*, 2031–
737 2044.

738 Ramsay, H., and A. Sobel (2011), Effects of relative and absolute sea surface temperature
739 on tropical cyclone potential intensity using a single-column model, *J. Clim.*, *24*, 183–
740 193.

741 Raymond, D., and X. Zeng (2005), Modelling tropical atmospheric convection in the
742 context of the weak temperature gradient approximation, *Q. J. R. Meteorol. Soc.*, *131*,
743 1301–1320.

744 Raymond, D. J., S. L. Sessions, A. H. Sobel, and Ž. Fuchs (2009), The mechanics of gross
745 moist stability, *J. Adv. Model. Earth. Syst.*, *1*.

746 Romps, D. (2012a), Weak pressure gradient approximation and its analytical solutions,
747 *J. Atmos. Sci.*, *69*, 2835–2845.

748 Romps, D. M. (2012b), Numerical tests of the weak pressure gradient approximation, *J.*
749 *Atmos. Sci.*, *69*, 2846–2856.

750 Schmidt, G. A., et al. (2014), Configuration and assessment of the GISS modele2 contri-
751 butions to the CMIP5 archive, *J. Adv. Model. Earth. Syst.*, *6*, 141–184.

- 752 Sessions, S., S. Sugaya, D. Raymond, and A. Sobel (2010), Multiple equilibria in a cloud-
753 resolving model using the weak temperature gradient approximation, *J. Geophys. Res.*,
754 *115*, D12,110.
- 755 Sessions, S. L., M. J. Herman, and S. Sentić (2015), Convective response to changes in
756 the thermodynamic environment in idealized weak temperature gradient simulations, *J.*
757 *Adv. Model. Earth. Syst.*
- 758 Shutts, G., and M. Gray (1994), A numerical modelling study of the geostrophic adjust-
759 ment process following deep convection, *Q. J. R. Meteorol. Soc.*, *120*, 1145–1178.
- 760 Skamarock, W. C., J. B. Klemp, J. Dudhia, D. O. Gill, D. M. Barker, W. Wang, and
761 J. G. Powers (2008), A description of the advanced research WRF version 3, *Tech. rep.*,
762 DTIC Document.
- 763 Sobel, A., and C. Bretherton (2000), Modeling tropical precipitation in a single column,
764 *J. Clim.*, *13*, 4378–4392.
- 765 Sobel, A., G. Bellon, and J. Bacmeister (2007), Multiple equilibria in a single-column
766 model of the tropical atmosphere, *Geophys. Res. Lett.*, *34*, L22,804.
- 767 Sobel, A. H., S. E. Yuter, C. S. Bretherton, and G. N. Kiladis (2004), Large-scale Me-
768 teorology and Deep Convection during TRMM KWAJEX, *Mon. Weather Rev.*, *132*,
769 422–444.
- 770 Tompkins, A. (2000), The impact of dimensionality on long-term cloud-resolving model
771 simulations, *Mon. Weather Rev.*, *128*, 1521–1535.
- 772 Tompkins, A. (2001), Organization of tropical convection in low vertical wind shears:
773 The role of water vapor, *J. Atmos. Sci.*, *58*, 529–545.

- 774 Vincent, D. (), The south Pacific convergence zone (spcz): A review, *Mon. Weather Rev.*,
775 *122*.
- 776 Voldoire, A., et al. (2013), The CNRM-CM5. 1 global climate model: description and
777 basic evaluation, *Clim. Dyn.*, *40*, 2091–2121.
- 778 Wang, S., and A. Sobel (2011), Response of convection to relative sea-surface tempera-
779 ture: Cloud-resolving simulations in two and three dimensions, *J. Geophys. Res.*, *116*,
780 D11,119.
- 781 Wang, S., and A. Sobel (2012), Impact of imposed drying on deep convection in a cloud-
782 resolving model, *J. Geophys. Res.*, *117*.
- 783 Wang, S., A. H. Sobel, and Z. Kuang (2013), Cloud-resolving simulation of TOGA-
784 COARE using parameterized large-scale dynamics, *J. Geophys. Res.*, *118*, 6290–6301.
- 785 Xu, K.-M., R. T. Cederwall, L. J. Donner, W. W. Grabowski, F. Guichard, et al. (2002),
786 An intercomparison of cloud-resolving models with the Atmospheric Radiation Mea-
787 surement summer 1997 intensive observation period data, *Q. J. R. Meteorol. Soc.*, *128*,
788 593–624.

Model type	Cloud-Resolving Models (CRMs)				
Modelling group	Columbia University	CNRM-GAME	NASA	New Mexico Tech	UK Met Office
Model ID	WRF	MesoNH	LaRC-CRM	NMTCMv3	LEMv2.4
Symbol	●	▲	◆	■	▼
Dimension	3D	3D	2D	2D	2D
Hor. size (km)	190 × 190	150 × 150	256	200	128
Hor. res (km)	2 × 2	3 × 3	4	1	0.5
P_{Ref} (mm d ⁻¹)	4.71	4.63	4.60	4.35	4.82

Table 1. List of cloud-resolving models (CRMs) that participated in this study. The symbols serve as a legend for results presented in Section 4. P_{Ref} is the mean precipitation rate obtained in the radiative-convective equilibrium simulation of each CRM with an SST of 300 K.

Model type	Single-Column Models (SCMs)						
Modelling group	LMD/IPSL		NASA	CNRM-GAME	UK Met Office	Koninklijk Nederlands Meteorologisch Insituut	
Model ID	LMDzA	LMDzB	GISS-SCM	ARPEGEv6 (ARPV6)	UMv7.8	EC-Earthv1	EC-Earthv3
Symbol	◁	▷	○	▽	★	◇	□
P_{Ref} (mm d ⁻¹)	4.38	4.39	4.58	3.71	4.76	4.53	4.15

Table 2. *List of single-column models (SCMs) that participated in this study. The symbols serve as a legend for results presented in Section 4. P_{Ref} is the mean precipitation rate obtained in the radiative-convective equilibrium simulation of each SCM with an SST of 300 K.*

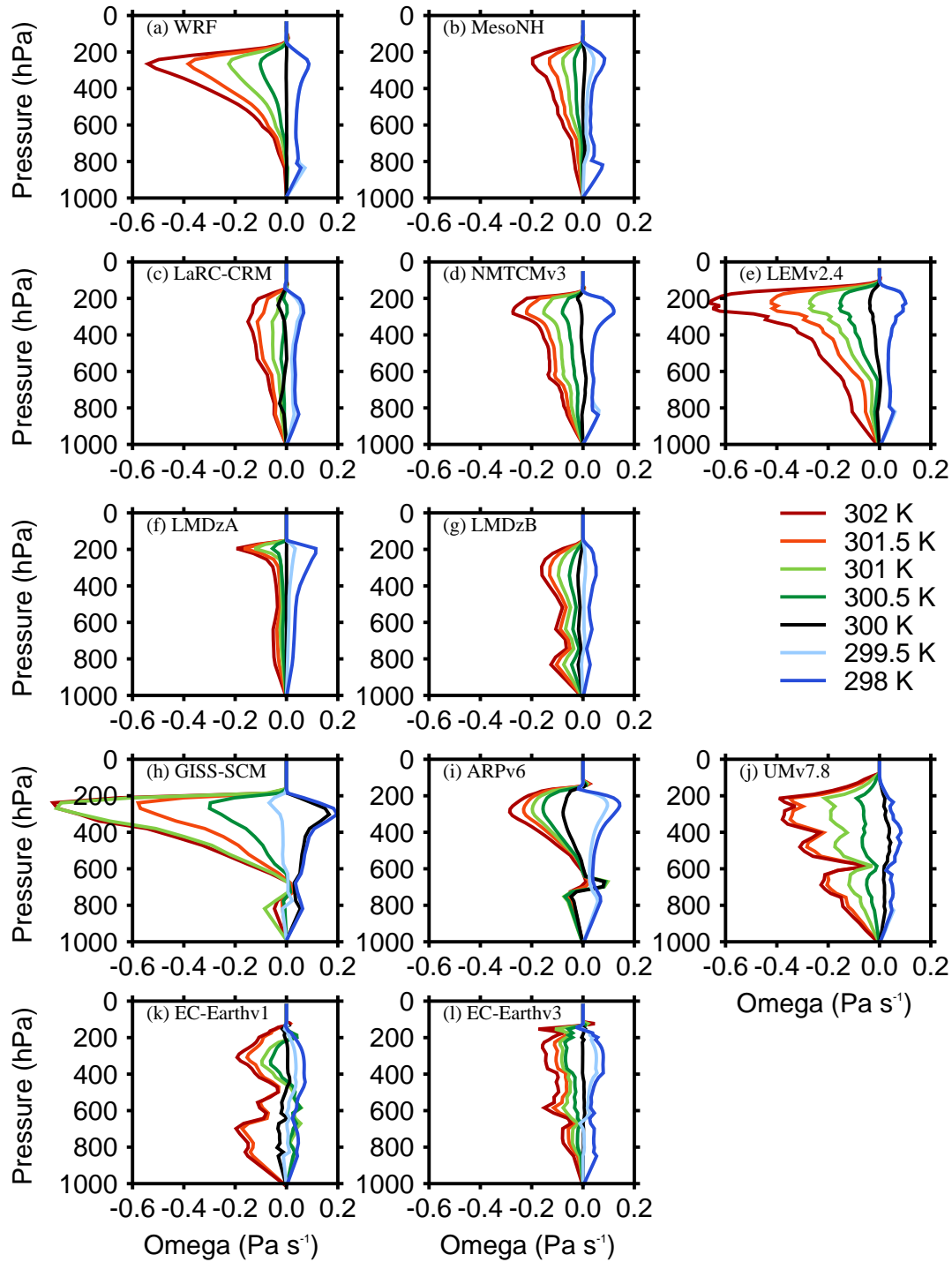


Figure 1. Large-scale pressure velocities obtained at equilibrium in the WTG simulations with an SST of 298 K (dark blue), 299.5 K (light blue), 300 K (black), 300.5 K (dark green), 301 K (light green), 301.5 K (orange), 302 K (red). Results are shown for the (a, b, c, d and e) CRMs and (f, g, h, i, j, k and l) SCMs. For each model, the reference profiles are their own RCE profiles at 300 K.

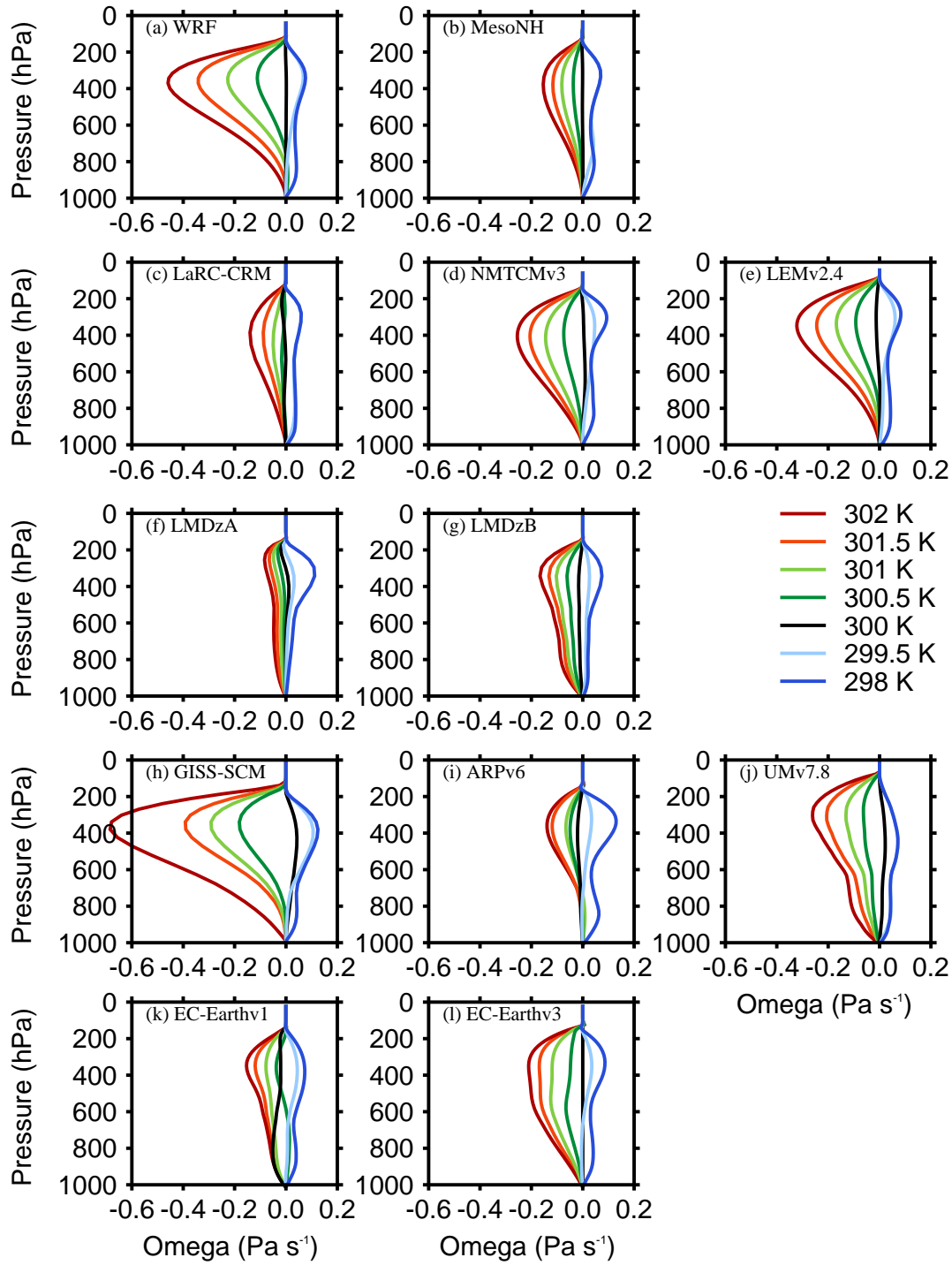


Figure 2. As in Figure 1, but for the equilibrium in the DGW simulations.

Model-CRMs	WTG or DGW	P/P_{Ref} or Ω	SST= 298 K	SST= 299.5 K	SST= 300 K	SST= 300.5 K	SST= 301 K	SST= 301.5 K	SST= 302 K
WRF	WTG	P/P_{Ref}	0.000	0.000	1.020	1.610	2.370	3.330	4.240
		Ω	-4.210	-4.420	0.180	2.990	6.670	11.230	15.520
	DGW	P/P_{Ref}	0.000	0.420	1.008	1.950	3.350	5.100	6.970
		Ω	-4.089	-2.575	0.110	4.180	9.485	15.547	22.235
MesoNH	WTG	P/P_{Ref}	0.002	0.529	0.896	1.303	1.714	2.220	2.857
		Ω	-4.079	-1.577	-0.290	1.391	3.176	5.221	7.839
	DGW	P/P_{Ref}	0.009	0.015	0.970	1.425	2.073	2.594	3.190
		Ω	-3.739	-3.461	0.060	1.803	4.145	6.0356	8.113
LaRC-CRM	WTG	P/P_{Ref}	0.006	0.276	1.200	1.233	1.908	2.824	3.322
		Ω	-3.549	-2.621	0.970	0.887	2.994	6.111	7.856
	DGW	P/P_{Ref}	0.000	0.084	1.102	1.233	1.757	2.394	3.282
		Ω	-3.563	-3.293	0.610	0.794	2.555	4.671	7.558
NMTCMv3	WTG	P/P_{Ref}	0.000	0.001	1.028	1.830	2.679	3.352	3.912
		Ω	-4.517	-4.621	0.100	3.303	6.570	9.221	11.317
	DGW	P/P_{Ref}	0.000	0.445	0.896	1.954	3.090	4.044	4.887
		Ω	-4.291	-2.266	-0.388	3.696	7.665	11.073	13.917
LEMv2.4	WTG	P/P_{Ref}	0.000	0.000	1.240	1.886	2.997	4.159	6.124
		Ω	-4.588	-4.668	1.110	5.471	9.745	15.162	24.048
	DGW	P/P_{Ref}	0.000	0.413	1.117	1.923	2.888	3.953	5.111
		Ω	-4.460	-2.658	0.464	4.129	8.103	12.436	17.031

Table 3. Table showing the numerical values of Ω ($\times 10^{-2} Pa s^{-1}$) and P/P_{Ref} for WTG and DGW simulations with different values of SST in the simulated column. Results in bold correspond to $|\Omega| < 0.4 \times 10^{-2} Pa s^{-1}$ (or $\bar{\omega} \approx 0$) or $0.9 < P/P_{Ref} < 1.1$. If both Ω and P/P_{Ref} are bold, the simulation with large-scale parameterization reproduces the RCE state to a good approximation.

Model-SCMs	WTG or DGW	P/P_{Ref} or Ω	SST= 298 K	SST= 299.5 K	SST= 300 K	SST= 300.5 K	SST= 301 K	SST= 301.5 K	SST= 302 K
LMDzA	WTG	P/P_{Ref}	0.176	0.790	0.997	1.313	1.520	1.829	2.192
		Ω	-4.071	-1.037	-0.015	1.385	2.240	3.387	4.806
	DGW	P/P_{Ref}	0.15	0.804	0.982	1.187	1.530	1.874	2.201
		Ω	-4.145	-0.972	-0.065	0.931	2.169	3.437	4.652
LMDzB	WTG	P/P_{Ref}	0.362	0.929	1.290	1.694	2.273	2.729	3.127
		Ω	-2.670	-0.30	1.180	2.992	5.475	7.470	9.193
	DGW	P/P_{Ref}	0.248	0.638	1.269	1.922	2.537	2.940	3.437
		Ω	-3.325	-1.462	1.030	3.676	6.153	7.726	9.689
GISS-SCM	WTG	P/P_{Ref}	0.044	1.200	0.180	3.325	4.161	2.833	5.605
		Ω	-6.888	1.100	-5.700	7.371	24.25	14.760	25.022
	DGW	P/P_{Ref}	0.021	0.330	0.820	2.201	3.498	4.319	8.296
		Ω	-6.095	-4.395	-2.180	7.566	12.837	17.475	34.335
ARPV6	WTG	P/P_{Ref}	0.003	0.000	1.530	1.920	2.067	2.132	2.368
		Ω	-5.486	-3.852	2.230	5.055	6.132	7.210	8.658
	DGW	P/P_{Ref}	0.000	0.832	1.260	1.442	1.464	2.098	2.223
		Ω	-5.853	-1.122	0.972	2.046	2.340	5.0256	5.673
UMv7.8	WTG	P/P_{Ref}	0.022	0.036	0.470	2.228	4.002	6.129	6.743
		Ω	-4.528	-4.600	-2.130	4.053	10.751	18.537	20.610
	DGW	P/P_{Ref}	0.003	0.0343	0.700	2.257	3.350	4.534	5.623
		Ω	-4.465	-4.437	-1.240	3.875	7.734	12.104	15.878
EC-Earthv1	WTG	P/P_{Ref}	0.011	0.792	1.420	0.529	0.558	3.682	4.101
		Ω	-4.060	-1.262	0.990	-0.741	-0.192	9.275	10.855
	DGW	P/P_{Ref}	0.002	0.662	1.920	1.024	2.271	2.807	3.170
		Ω	-4.117	-1.737	2.990	0.583	4.713	6.736	8.187
EC-Earthv3	WTG	P/P_{Ref}	0.003	0.577	0.940	1.720	2.202	2.648	3.430
		Ω	-4.209	-1.860	-0.135	2.927	4.611	6.008	8.523
	DGW	P/P_{Ref}	0.0122	0.813	1.014	2.191	3.448	4.344	5.087
		Ω	-4.280	-0.986	0.146	3.873	8.138	11.061	13.460

Table 4. Same as Table 3, but lists SCM results.

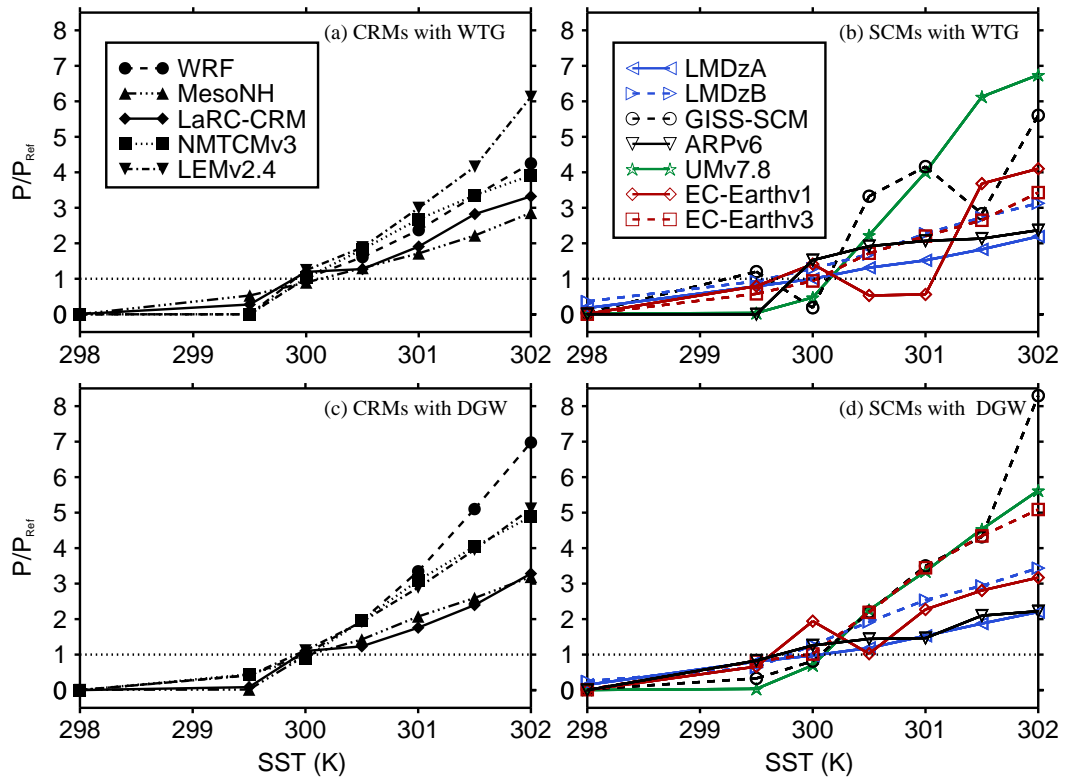


Figure 3. P/P_{Ref} versus SST. The values of P are those obtained at equilibrium in the (top) WTG and (bottom) DGW simulations. Results are shown for (left) CRMs and (right) SCMs. Symbol definitions are as in Tables 1 and 2.

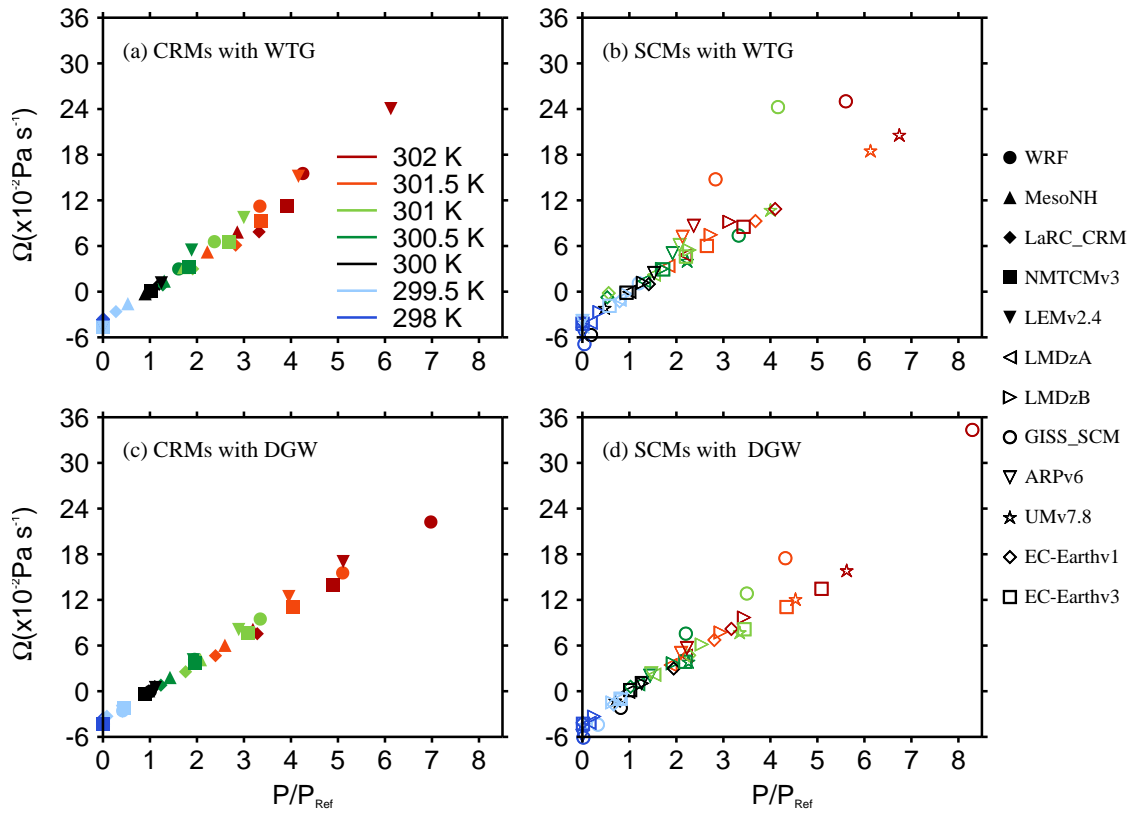


Figure 4. Scatter plots of Ω versus P/P_{Ref} . Results are those obtained at equilibrium in the (top) WTG and (bottom) DGW simulations with an SST of 298 K (dark blue), 299.5 K (light blue), 300 K (black), 300.5 K (dark green), 301 K (light green), 301.5 K (orange), and 302 K (red). Results are shown for (left) CRMs and (right) SCMs. Symbol definitions are as in Tables 1 and 2.

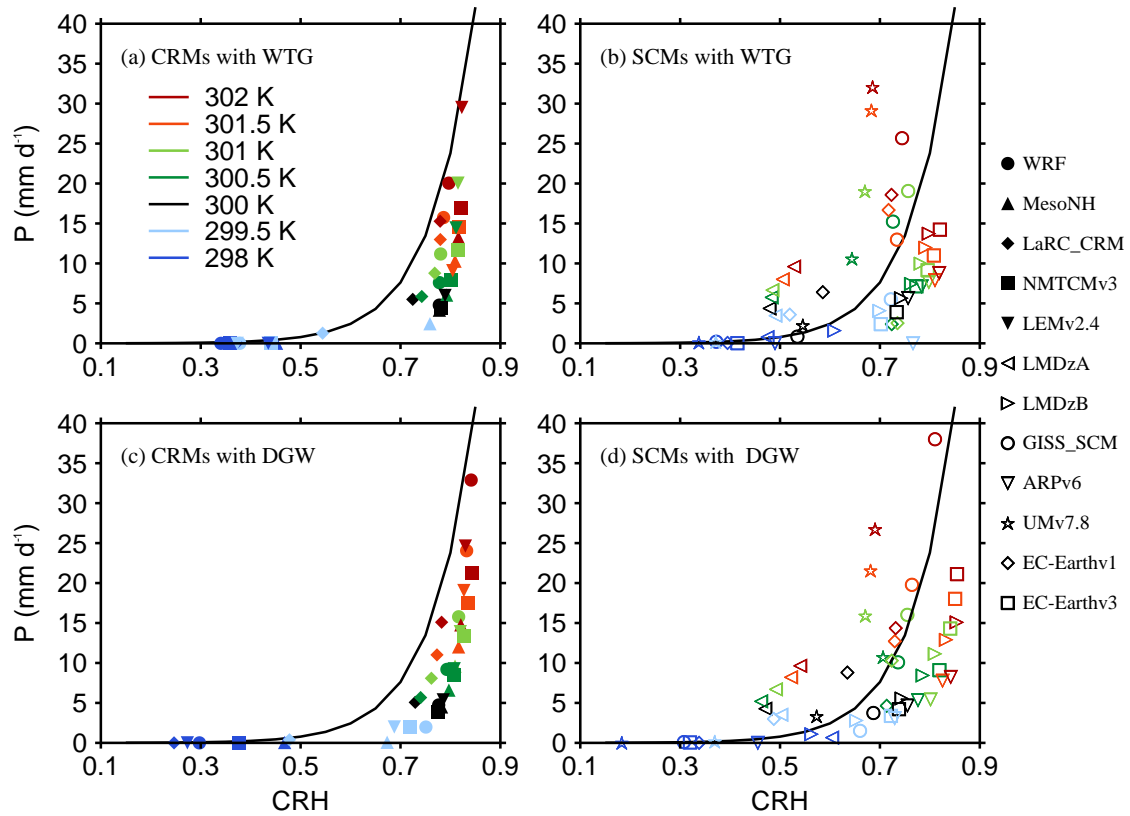


Figure 5. Scatter plots of P versus CRH (column relative humidity; the column-integrated water vapor divided by its saturation value). The results are those obtained at equilibrium in the (top) WTG and (bottom) DGW simulations with an SST of 298 K (dark blue), 299.5 K (light blue), 300 K (black), 300.5 K (dark green), 301 K (light green), 301.5 K (orange), and 302 K (red). Results are shown for (left) CRMs and (right) SCMs. Symbol definitions are as in Tables 1 and 2. The solid curve is the exponential fit for the observed monthly mean precipitation over the tropical oceans obtained by Bretherton et al. [2004].

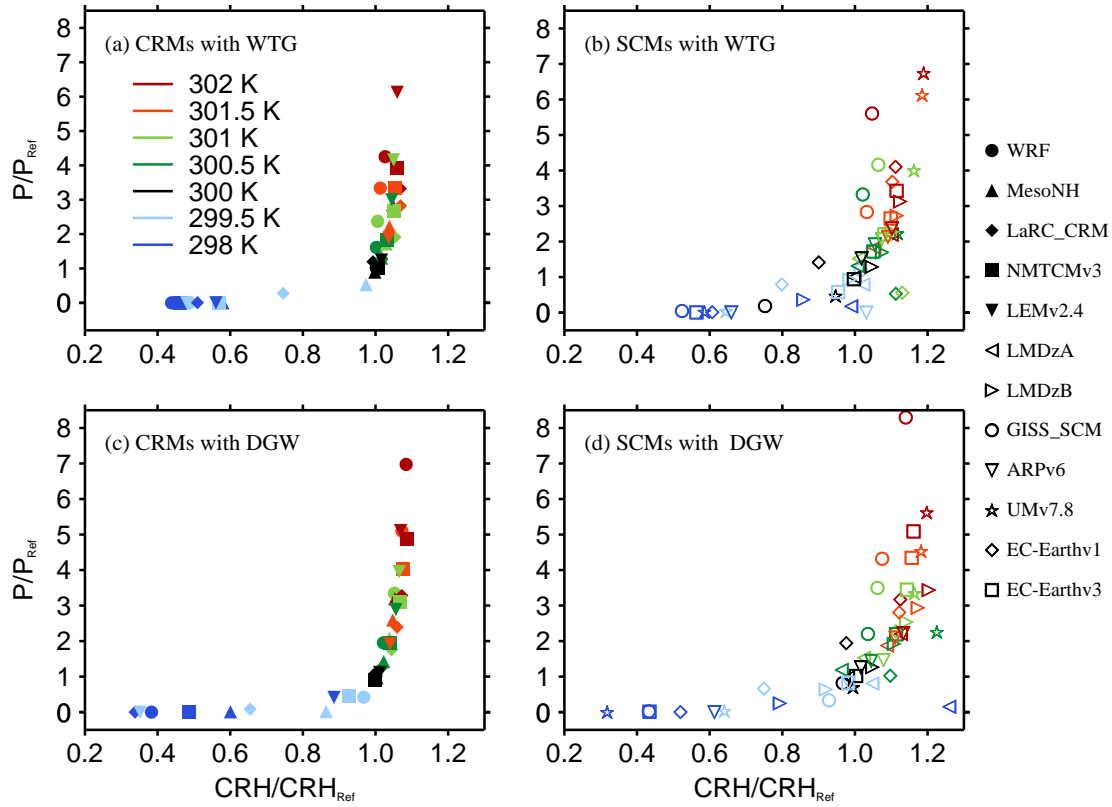


Figure 6. Scatter plots of P/P_{Ref} versus CRH/CRH_{Ref} , where CRH_{Ref} is the column relative humidity of the corresponding RCE reference state. The results are those obtained at equilibrium in the (top) WTG and (bottom) DGW simulations with an SST of 298 K (dark blue), 299.5 K (light blue), 300 K (black), 300.5 K (dark green), 301 K (light green), 301.5 K (orange), and 302 K (red). Results are shown for (left) CRMs and (right) SCMs. Symbol definitions are as in Tables 1 and 2.

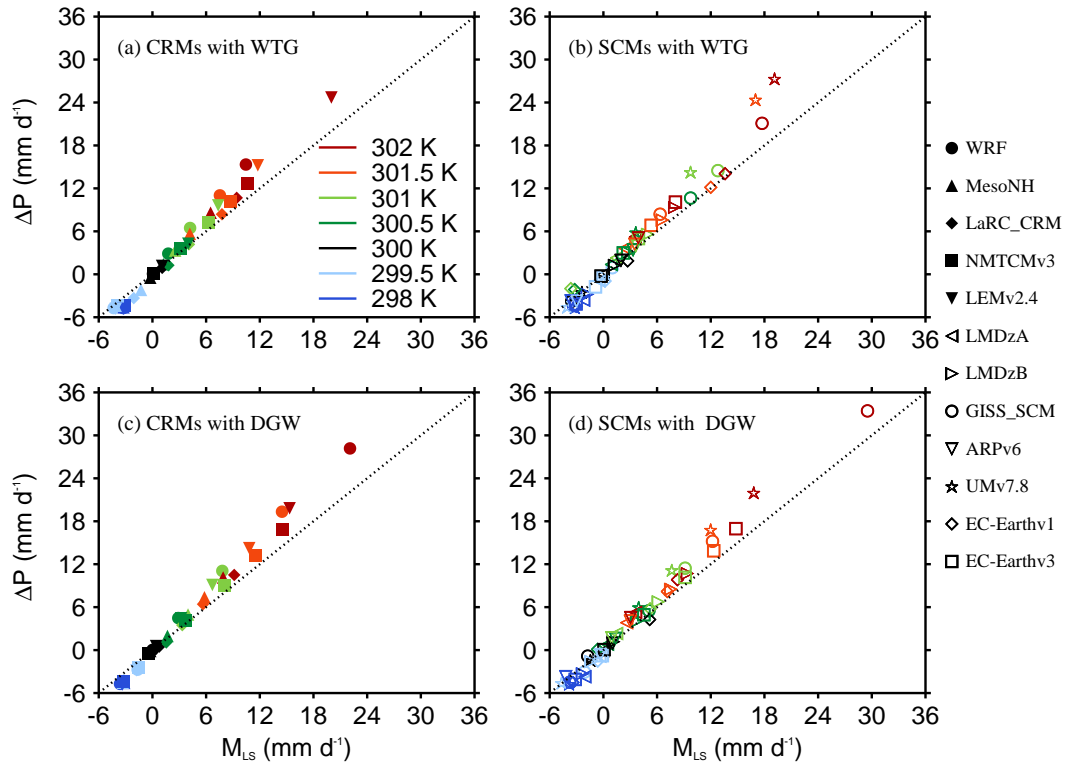


Figure 7. Scatter plots of ΔP versus M_{LS} . The results are those obtained at equilibrium in the (top) WTG and (bottom) DGW simulations with an SST of 298 K (dark blue), 299.5 K (light blue), 300 K (black), 300.5 K (dark green), 301 K (light green), 301.5 K (orange), and 302 K (red). Results are shown for (left) CRMs and (right) SCMs. The dotted oblique line corresponds to $\Delta P = M_{LS}$. Symbol definitions are as in Tables 1 and 2.

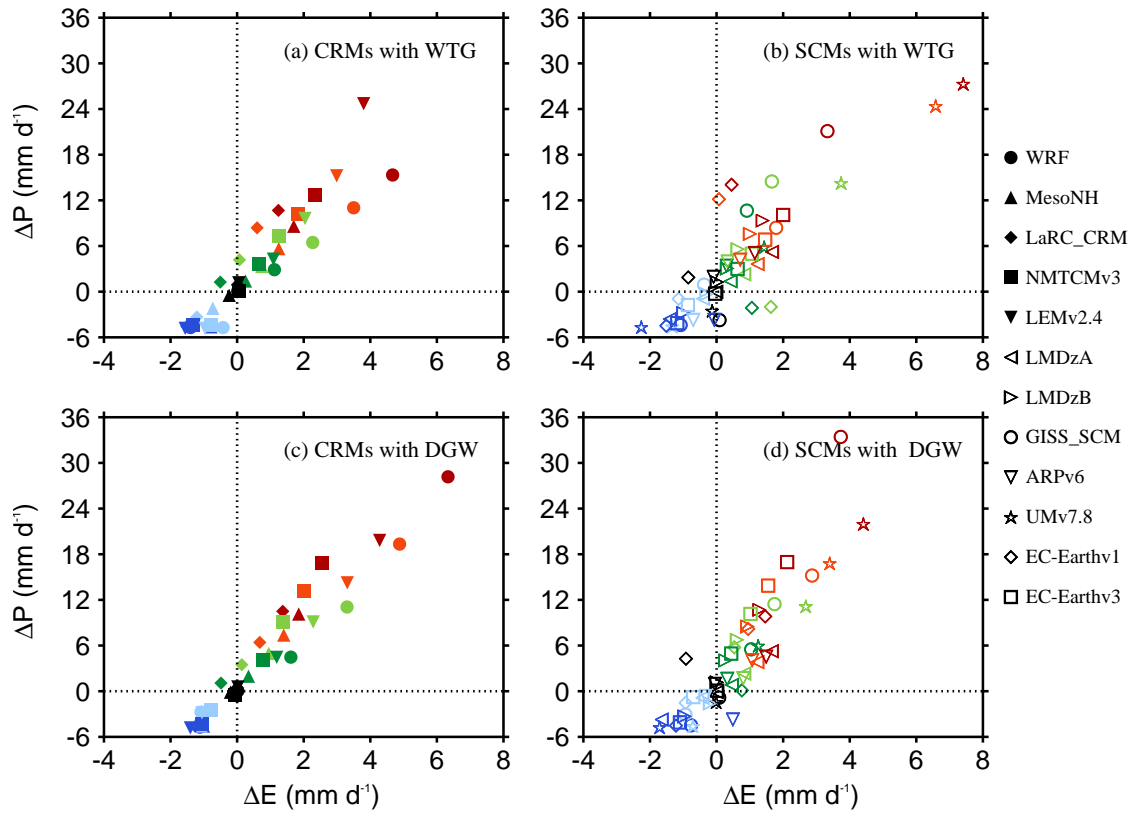


Figure 8. Scatter plots of ΔP versus ΔE . Results are those obtained at equilibrium in the (top) WTG and (bottom) DGW simulations over an SST of 298 K (dark blue), 299.5 K (light blue), 300 K (black), 300.5 K (dark green), 301 K (light green), 301.5 K (orange), and 302 K (red). Results are shown for (left) CRMs and (right) SCMs. Symbol definitions are as in Tables 1 and 2.

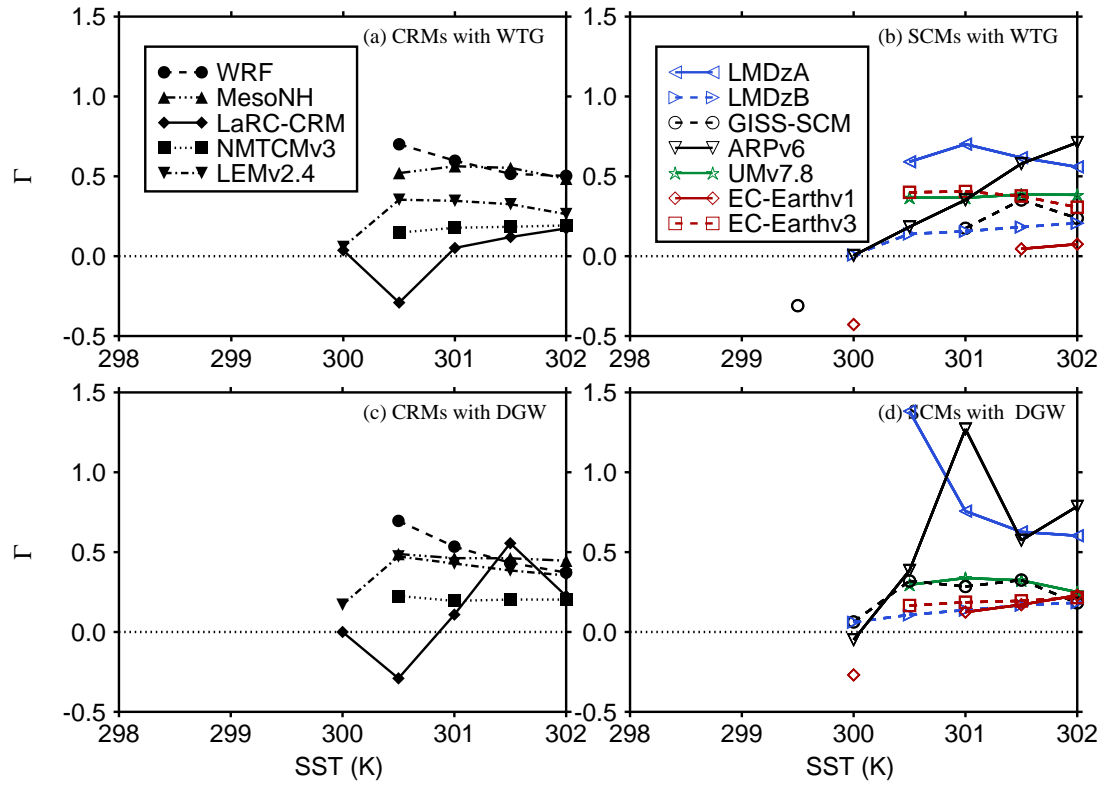


Figure 9. Γ versus SST. The values of Γ are those obtained at equilibrium in the (top) WTG and (bottom) DGW simulations which produce significant large-scale ascent only ($P/P_{Ref} > 1.1$ with $\Omega > 0.4 \times 10^{-2} \text{ Pa s}^{-1}$). Results are shown for (left) CRMs and (right) SCMs. Symbol definitions are as in Tables 1 and 2.